The University of Manchester Research

Reactivity Differences of Trigonal Pyramidal Nonheme Iron(IV)-Oxo and Iron(III)-Oxo Complexes: Experiment and Theory.

Document Version
Accepted author manuscript

[Link to publication record in Manchester Research Explorer](#)

FULL PAPER

Reactivity Differences of Trigonal Pyramidal Nonheme Iron(IV)-Oxo and Iron(III)-Oxo Complexes: Experiment and Theory.

Yuanxin Cao,[a,b] Juan A. Valdez-Moreira,[c] Sam Hay,[a,b] Jeremy M. Smith,*[c] and Sam P. de Visser*[a,d]

[a] Mr Y. Cao, Prof S. Hay, Dr S. P. de Visser
Manchester Institute of Biotechnology
The University of Manchester
131 Princess Street, Manchester M1 7DN, United Kingdom
E-mail: sam.devisser@manchester.ac.uk

[b] Mr. Y. Cao, Prof. S. Hay
Department of Chemistry
The University of Manchester
Oxford Road, Manchester M13 9PL, United Kingdom

[c] Dr. J.A. Valdez-Moreira, Prof J. M. Smith
Department of Chemistry
Indiana University
Bloomington, Indiana 47405, United States
E-mail: smith962@indiana.edu
URL: https://www.chem.indiana.edu/faculty/jeremy-smith/

[d] Dr. S. P. de Visser
Department of Chemical Engineering
The University of Manchester
Oxford Road, Manchester M13 9PL, United Kingdom
URL: https://research.manchester.ac.uk/en/persons/sam.devisser

Supporting information for this article is given via a link at the end of the document.

Abstract: High-valent metal-oxo species play critical roles in enzymatic catalysis yet their properties are still poorly understood. In this work we report a combined experimental and computational study into biomimetic iron(IV)-oxo and iron(III)-oxo complexes with tight second-coordination sphere environments that restrict substrate access. The work shows that the second-coordination sphere slows the hydrogen atom abstraction step from toluene dramatically and the kinetics is zeroth order in substrate. However, the iron(II)-hydroxo that is formed has a low reduction potential and hence cannot do OH rebound favorably. The tolyl radical in solution then reacts further with alternative reaction partners. By contrast, the iron(IV)-oxo species reacts predominantly through OH rebound to form alcohol products. Our studies show that the oxidation state of the metal influences reactivities and selectivities with substrate dramatically and that enzymes will likely need an iron(IV) center to catalyze C−H hydroxylation reactions.

Introduction

High-valent metal-oxo species are common reaction intermediates in enzyme-catalyzed reactions of a large variety of mono-oxygenases and dioxygenases.[1,2] For instance, in the nonheme iron and α-ketoglutarate-dependent dioxygenases dioxygen reacts on an iron active site with bound α-ketoglutarate to form an iron(IV)-oxo species.[3] The latter was trapped and characterized for several proteins using a combination of spectroscopic techniques.[4] Furthermore, the iron(IV)-oxo species was found to react efficiently with substrates through aliphatic C−H hydrogen atom abstraction leading to substrate hydroxylation, although there is also evidence of desaturation reactions.[5] Nevertheless, many questions on the high selectivity and specificity of these enzyme intermediates still remain to be

resolved. To gain further insight into the nature and chemical properties of enzymatic catalytic cycle intermediates, and particularly their electronic configuration, the effect of ligands and second-coordination sphere effects on their structure and reactivity, biomimetic (synthetic) models have been synthesized. Many biomimetic iron(IV)-oxo species have been trapped and characterized spectroscopically and crystallographically.[6] In addition, reactivity patterns with model substrates were explored for substrate hydroxylation, desaturation, sulfoxidation and epoxidation and versatile reaction patterns have been studied.[7] The work has given insight into chemical and biological catalysis and revealed structure and property relationships.

A much lesser studied system than the iron(IV)-oxo species is its one-electron reduced form, namely the iron(III)-oxo species. Several studies reported crystallographic and spectroscopic characterization of biomimetic iron(III)-oxo complexes in solution and their reactivity patterns with substrates with weak C−H bonds.[8] Most of these complexes, however, have the oxo group locked in position through internal hydrogen bonding interactions with N−H groups of the ligand framework, thereby restricting substrate approach and reactivity. Roithová and co-workers[9] trapped and characterized a number of biomimetic iron(III)-oxo species in the gas-phase and measured Fe−O frequencies at low pressure in the gas-phase of ^{16}O and ^{18}O-containing complexes. They highlighted a wide spread of Fe−O stretch vibrations that was shown to be dependent on the ligand structure, coordinate environment and the overall spin multiplicity. Moreover, a correlation between experimentally measured Fe−O stretch vibration and bond length was obtained.

Recently, some of us synthesized and characterized the [PhB(AdIm)$_3$Fe^{III}=O] complex, Ad = adamantyl and Im = imidazol-2-ylidene, designated $\mathbf{1}_{III}$ as shown in Scheme 1.[10] The crystallographically determined structure highlighted a short Fe−O distance of 1.633 Å and an almost linear B−Fe−O angle of

FULL PAPER

178.15°. The carbene-iron distances range from 1.933 – 1.952 Å. The system does not display hydrogen bonding interactions to the oxo group, but has a large second-coordination sphere environment due to the adamantyl substituents. Further spectroscopic characterization identified an 858 cm^{-1} Fe–O stretching vibration in the infrared (IR) spectrum and an overall doublet spin state from electron paramagnetic resonance (EPR) measurements. The complex was found to react with toluene to give a set of unusual products, namely the iron(II)-hydroxo complex and an iron(II)-benzoxy complex (Scheme 1).
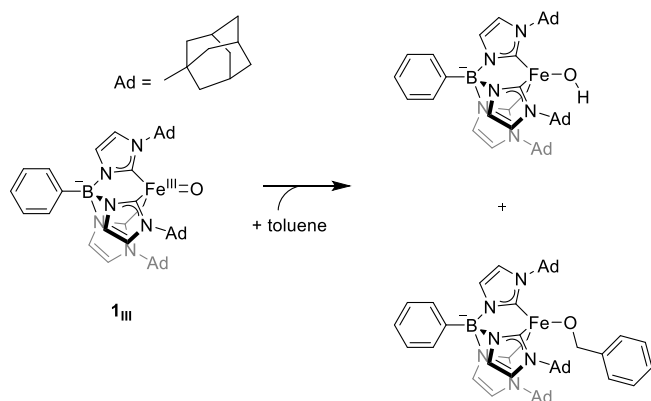
Scheme 1. Reaction products observed for the reaction of a biomimetic iron(III)-oxo species (**1**$_{III}$) with toluene.

However, it is not clear how these products are obtained, why no substrate hydroxylation occurs, what the effect of the adamantyl groups is and what the difference in reactivity with an iron(IV)-oxo species would be. Moreover, the corresponding iron(IV)-oxo complex has never been made and studied. To answer these questions, we performed additional kinetic measurements along with a detailed density functional theory study on the [PhB(AdIm)$_3$Fe^{III}=O] (**1**$_{III}$) and [PhB(AdIm)$_3$Fe^{IV}=O]$^+$ (**1**$_{IV}^+$) species and their reactivity with toluene and substituted methylbenzenes. The work shows that due to steric interactions of the adamantyl substituents substrate approach to the iron(III)-oxo is hampered. In addition, the iron(II)-hydroxo that is formed cannot do the OH rebound step as it is energetically costly. As such, the tolyl radical is released into solution and reacts with another iron(III)-oxo species to form the iron(II)-benzoxy complex. By contrast, we predict that the corresponding iron(IV)-oxo species will have much lower OH rebound barriers and will preferentially hydroxylate toluene. Our studies show how the second-coordination sphere effects influence reactivity, kinetics as well as well as selectivities of chemical reactions. In particular, an iron(III)-oxo species can only catalyze a single hydrogen atom abstraction reaction, while an iron(IV)-oxo species reacts predominantly via a two-electron transfer process with substrates to give alcohols, epoxides or sulfoxides.

Results and Discussion

In this report we expanded our substrate scope from our previous work with further experimental studies and measured the kinetics for the reaction of **1**$_{III}$ with substituted toluenes. Additional computational work explored the structure and mechanism of the

reactivity of the iron(III)-oxo complex (**1**$_{III}$) with toluene. To gain further insight into the catalytic potential of **1**$_{III}$ we expanded the calculations with the mechanism and reactivity of the corresponding iron(IV)-oxo species (**1**$_{IV}^+$), as well as a truncated model with the adamantyl substituents removed (**1**$_{NOAD}$).

Kinetics studies

We previously reported that no kinetic isotope effect was observed for the reaction of **1**$_{III}$ and toluene and toluene-d$_8$.[10] Here we report the results of further kinetic studies into the reaction between **1**$_{III}$ and toluene. The pseudo first-order rate constants for the reaction of **1**$_{III}$ (1.9 mM) with toluene in THF were determined by UV-vis spectroscopy at 60 °C. Surprisingly, the rate shows no dependence on toluene over the concentration range used (19 – 665 mM). While unusual, a zeroth-order dependence on substrate concentration has been observed for the reactions of other metal-oxo complexes.[11] As with previous work, we attribute this observation for the reaction of **1**$_{III}$ to a rapid association equilibrium that precedes a rate-determining hydrogen atom transfer:

$$FeO + C_7H_8 \rightleftharpoons [FeO \bullet C_7H_8] \qquad K_{12}$$
$$[FeO \bullet C_7H_8] \rightarrow FeOH + C_7H_7 \bullet \qquad k_3$$
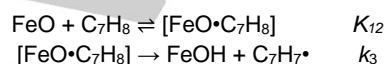
with rate constant:

The zeroth-order dependence on toluene concentration likely stems from a large association constant ($K_{12}[C_7H_8] \gg 1$), leading to $k_{exp} \cong k_3$. Consistent with the formation of an association

$$k_{exp} = \frac{k_3 K_{12}[C_7H_8]}{K_{12}[C_7H_8] + 1}$$

complex, we observe a 5 nm redshift in the visible band of the UV-Vis spectrum when the solvent is changed from THF to toluene (see Figure S6, Supporting Information).[12]
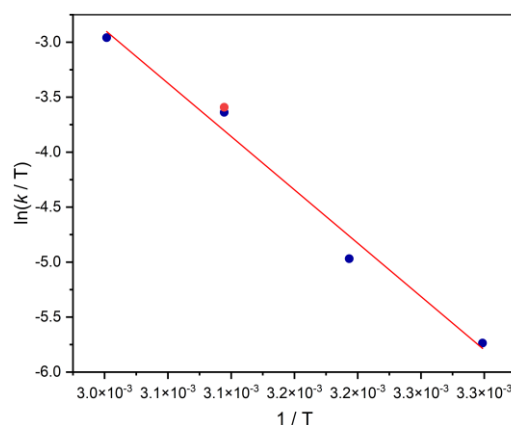
Figure 1. Eyring plot for the reaction of **1**$_{III}$ (initial concentration = 1.9 mM) and toluene. Temperature range = 30 – 60 °C. The rate of reaction with toluene-d$_8$ is plotted in red.

Subsequently, we measured the temperature dependence of the rate constants in an Eyring plot (Figure 1). An Eyring analysis of the temperature dependence of the rate constants provides

activation parameters for the hydrogen atom abstraction from toluene by $\mathbf{1}_{III}$.

π^*_{xy} π^*_{xz} π^*_{yz} σ^*_{z2} σ^*_{x2-y2}

$^2\mathbf{1}_{III}$ ($^4\mathbf{1}_{III}$)

$^{2,4}\mathbf{1}_{III}$ ($^4\mathbf{1}_{III}$)	B3LYP	PBE0	BP86
Fe-O [Å]	1.638 (1.656)	1.638 (1.644)	1.638 (1.667)
O-Fe-B [°]	178 (147)	178 (145)	178 (147)
ν_{FeO} [cm^{-1}]	867 (862)	890 (884)	866 (847)
ΔE+ZPE [kcal mol^{-1}]	1.9	1.6	2.1
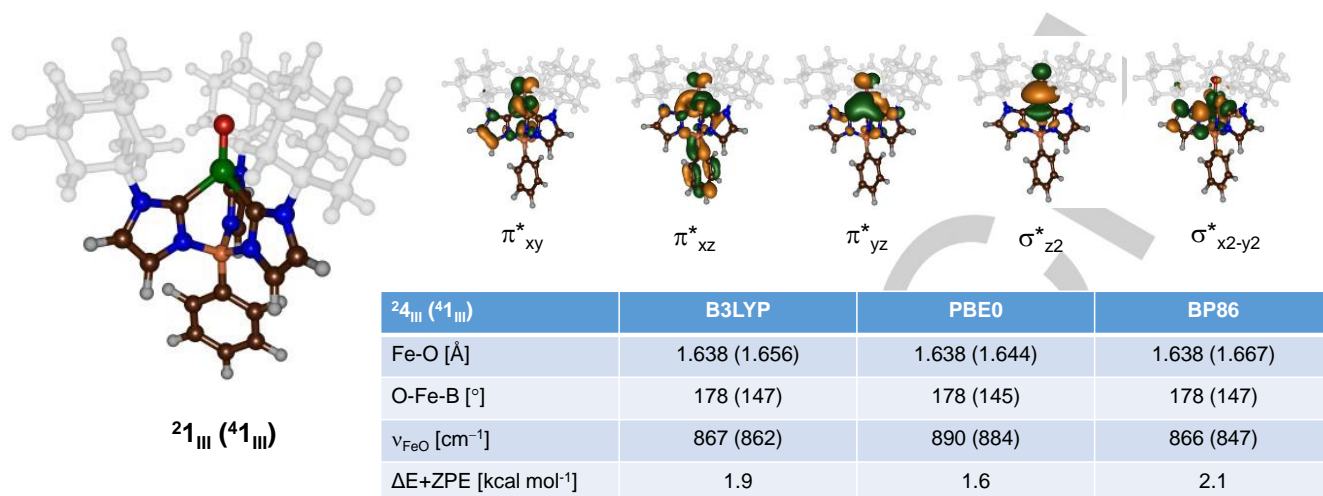
Figure 2. Optimized geometries of $^{2,4}\mathbf{1}_{III}$ as calculated using different density functional theory methods and key molecular orbital of $^{2,4}\mathbf{1}_{III}$. Distances are given in Å, angles in degrees, the Fe−O stretch vibration (ν_{FeO}) is in cm^{-1} and the spin-state energy relative to the doublet spin state (ΔE+ZPE value using BS2 energy and BS1 ZPE correction) is in kcal mol^{-1}.

From the slope and intercept of the curve in Figure 1 an enthalpy and entropy of activation for the reaction is determined. Values of $\Delta H^{\ddagger} = 19(1)$ kcal mol^{-1} and $\Delta S^{\ddagger} = 4.7(5)$ e.u. were obtained. These activation parameters correspond to a free energy of activation of $\Delta G^{\ddagger} = 20(1)$ kcal mol^{-1} at 298 K for the hydrogen atom abstraction from toluene by $\mathbf{1}_{III}$. We also investigated the rate of hydrogen atom abstraction for a series of *para*-substituted toluenes, Supporting Information Figure S5. The slope of the resulting Hammett plot shows that there is no electronic effect on the rate of reaction and virtually the same rate constant is obtained regardless of the nature of the *para*-substituent.

Structure and reactivity of $\mathbf{1}_{III}$.
Subsequently, density functional theory methods were applied to gain insight into the reaction mechanism of $\mathbf{1}_{III}$ with toluene and the product distributions. Our work started with a series of test calculations on the iron(III)-oxo complex $\mathbf{1}_{III}$ in all possible spin states (doublet and quartet) using various computational approaches. We particularly investigated the spin state ordering and the spectroscopic features of the various complexes and compared those with experimental observation. Figure 2 displays the optimized geometries of the doublet and quartet iron(III)-oxo complexes $^{4,2}\mathbf{1}_{III}$ and the relevant molecular valence orbitals as calculated with the B3LYP, PBE0 and BP86 density functional approaches and the same basis set (see Methods Section). Key valence orbitals are shown at the top of Figure 2, which are molecular orbitals with significant amount of metal 3d contributions, hence are labelled based on the iron 3d atomic orbital involved. The molecular valence orbitals are assigned as π^*_{xy}, π^*_{xz}, π^*_{yz}, σ^*_{z2} and σ^*_{x2-y2}, whereby the z-axis is taken along the Fe−O bond. The three π^* orbitals involve interactions of the metal $3d_{xy}$, $3d_{xz}$ and $3d_{yz}$ atomic orbitals with 2p orbitals on the oxygen atom. Further interactions of the carbon 2p orbitals of the imidazolylidene groups stabilize the π^* orbitals further. The σ^*_{z2} is the antibonding orbital along the Fe−O axis, while the σ^*_{x2-y2} is orthogonal to the z-axis, where the metal interacts with ligand 2p

orbitals. Regardless of the computational method used, we find a doublet spin ground state for $\mathbf{1}_{III}$ with electronic configuration $\pi^*_{xy}{}^2$ $\pi^*_{xz}{}^2$ $\pi^*_{yz}{}^1$. This is in agreement with experimental electron paramagnetic resonance (EPR) studies on $\mathbf{1}_{III}$ that found a doublet spin ground state.[10] The quartet spin state is higher lying by 1.9 kcal mol^{-1} at the UB3LYP/BS2//UB3LYP/BS1+ZPE (zero-point energy) level of theory. Using the PBE0 and BP86 approaches a doublet spin ground state is also found with the quartet spin state higher in energy by 1.6 and 2.1 kcal mol^{-1}, respectively. Therefore, the calculations appear to show little sensitivity in structure and spin state ordering when the computational approach is changed.
The B3LYP optimized structure in the doublet spin has the B−Fe−O entity almost co-linear at an angle of 178°, which matches the value obtained from the crystal structure coordinates (178.15°) excellently.[10] Furthermore, the calculated Fe−O distance and Fe−O stretch vibration are 1.638 Å and 867 cm^{-1}, respectively, again in excellent agreement with the crystal structure and IR spectroscopic characterizations.[10] Virtually the same chemical structure is obtained after a geometry optimization using either the PBE0 or BP86 methods, which shows that there is little sensitivity in the spin state ordering and orbital occupations, when a different computational approach is used. In the quartet spin state there is more variation in the Fe−O bond length and the shortest distance is found with PBE0 (1.644 Å), while with B3LYP and BP86 somewhat longer distances of 1.656 and 1.667 Å are obtained. The optimized geometries of the iron(III)-oxo species are, therefore, not dramatically different from previous reports on enzymatic and biomimetic iron(IV)-oxo complexes, where similar Fe−O distances were reported.[13,14] Interestingly, in the quartet spin state due to σ^*_{x2-y2} occupation with one electron, the B−Fe−O angle is considerably bent at 147°. However, the bending angle has little effect on the value of the Fe−O stretch vibration and in the quartet spin state it is 862 cm^{-1}, while the value at the doublet spin state at 867 cm^{-1}. The former is close to the one obtained experimentally at 858 cm^{-1}.

3
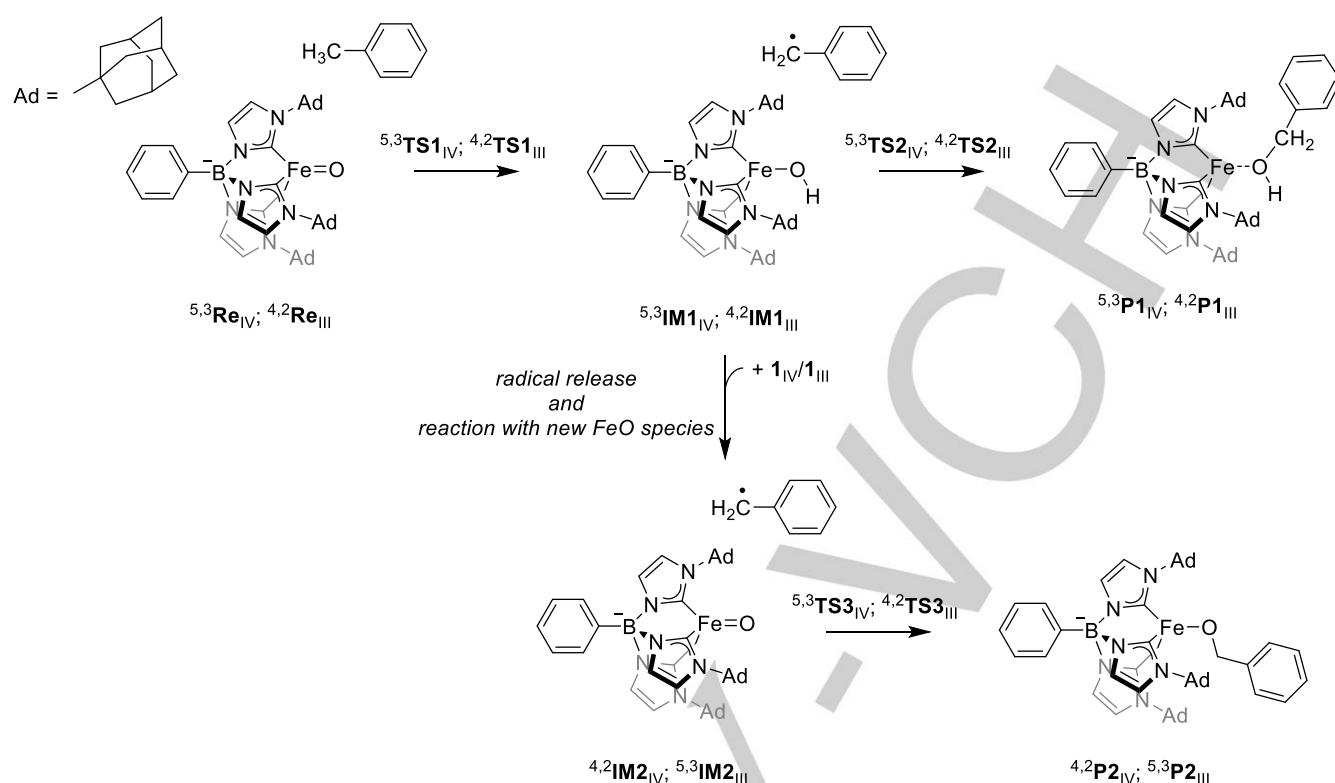
Scheme 2. Reaction mechanisms of toluene activation by iron(III)-oxo and iron(IV)-oxo complexes leading to phenylmethanol and benzoxy complex.

Using PBE0 the Fe−O stretch vibration is found at a significantly higher value of 890 cm^{-1}, whereas at the BP86 level of theory a frequency of 866 cm^{-1} is calculated.

To further test the reproducibility of the method, we calculated ^{57}Fe Mössbauer parameters of $^2\mathbf{1}_{III}$ using the B3LYP optimized geometry and find a quadrupole splitting of $\Delta E_Q = 1.95$ mm s^{-1} as compared to the experimental value of 1.94 mm s^{-1}.[10] Moreover, an isomer shift $\delta = -0.16$ mm s^{-1} was calculated, whereas experimentally -0.15 mm s^{-1} was measured. Consequently, the calculated structure and spectroscopic parameters calculated with B3LYP/BS1 are in excellent agreement with experimental observation. As the B3LYP density functional reproduced experimental data well, we continued with calculating the reaction mechanism for toluene activation by $^{2,4}\mathbf{1}_{III}$ and $^{1,3,5}\mathbf{1}_{IV}{}^+$, namely for the iron(III)-oxo and iron(IV)-oxo complexes with the PhB(AdIm$_3$) ligand. Thus, previous work on toluene activation by iron(IV)-oxo complexes highlighted a mechanism for initial hydrogen atom abstraction followed by OH rebound to give phenylmethanol products.[15] However, the experimental studies of $\mathbf{1}_{III}$ with toluene did not report hydroxylation products but instead an iron(II)-hydroxo and iron(II)-benzoxy complex were characterized. To understand this unusual product distribution we did a mechanistic DFT study on the pathways of toluene activation by iron(III)-oxo and iron(IV)-oxo complexes $\mathbf{1}_{III}$ and $\mathbf{1}_{IV}{}^+$ leading to the various products. Scheme 2 shows the reaction mechanisms and labelling nomenclature of the structures for our mechanistic investigation.

The iron-oxo complexes with toluene bound, i.e., the reactant complexes $\mathbf{Re}_{III}$ and $\mathbf{Re}_{IV}$ for the iron(III)-oxo and iron(IV)-oxo complexes, react via hydrogen atom abstraction with transition state **TS1** to form the radical intermediates **IM1** containing an iron-hydroxo and tolyl group. Usually, the hydrogen atom abstraction by an iron-oxo species is followed by OH rebound to form the corresponding alcohol,[15,16] i.e., they form the phenylmethanol product complexes **P1**, which we investigated via transition state **TS2**. However, we also considered radical release from **IM1** and its splitting into a separate iron-hydroxo species and C$_6$H$_5$CH$_2$$^\bullet$ radical. This radical can then react with another iron-oxo species to initially form the intermediate **IM2** prior to C−O bond formation via transition state **TS3**, ultimately yielding the benzoxy complexes **P2**. These pathways were explored for the iron(III)-oxo species and the iron(IV)-oxo species.

We initially created reactant complexes of weakly interacting $^{2,4}\mathbf{1}_{III}$ with toluene: $^{2,4}\mathbf{Re}_{III}$. Although for isolated reactants the doublet spin state is the ground state by ΔE+ZPE = 1.9 kcal mol^{-1} over the quartet spin state, in agreement with experiment, actually the spin state ordering reverses for the reactant complexes $\mathbf{Re}_{III}$. In particular, for the reactant complexes the quartet spin state is slightly below the doublet spin complex by ΔE+ZPE = 0.3 kcal mol^{-1} (Figure 3). We envisaged a spin state crossing and therefore searched for a minimum energy crossing point (MECP) between the doublet and quartet spin state surfaces. The MECP is slightly above the isolated reactant in the doublet spin state (by 0.4 kcal mol^{-1}) and its geometry is shown in Figure 3. The MECP structure is a non-covalently bound complex of the iron(III)-oxo species and toluene where the protons of the methyl group of the substrate for a weak hydrogen bonding interaction with the oxo group.

4
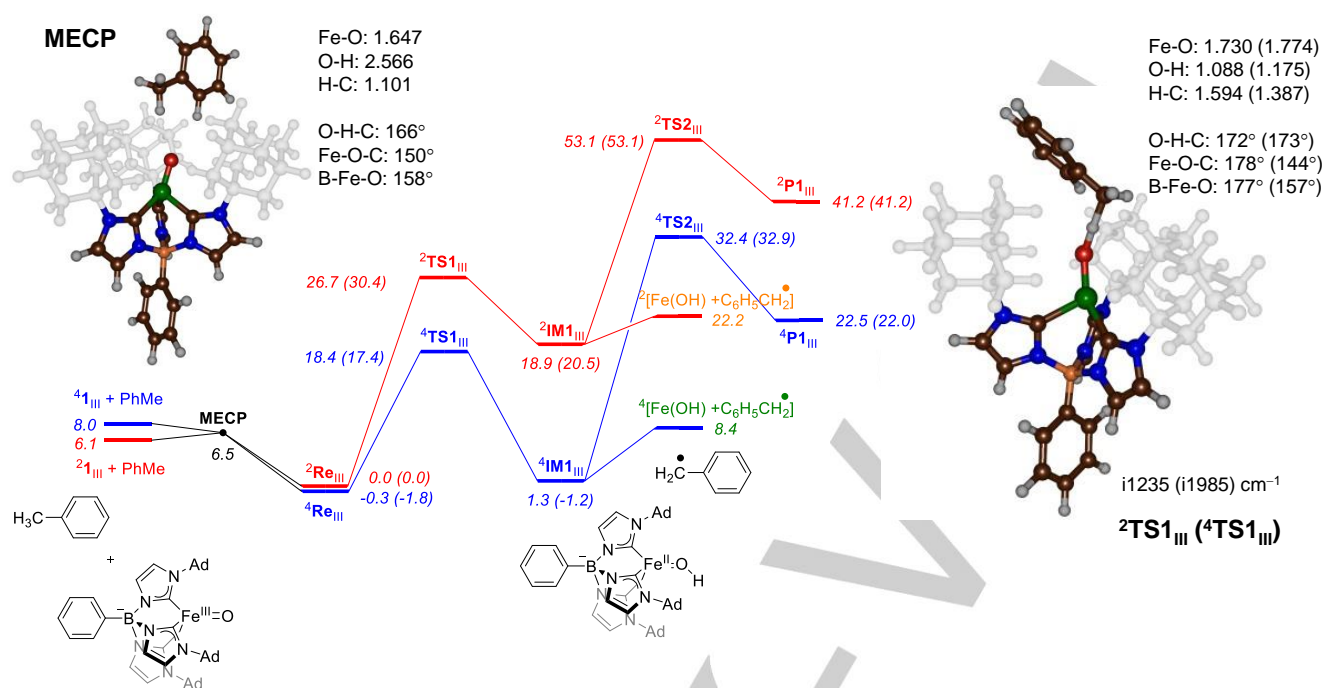
Figure 3. UB3LYP/BS2//UB3LYP/BS1 calculated potential energy landscape with $\Delta E+ZPE$ (ΔG) values in kcal mol^{-1} for hydrogen atom abstraction from toluene by $^{2,4}\mathbf{1}_{III}$. Also shown are optimized geometries of the MECP and transition state structures with bond lengths in angstroms, bond angles in degrees and the imaginary frequency in cm^{-1}. Free energies obtained at 298 K.
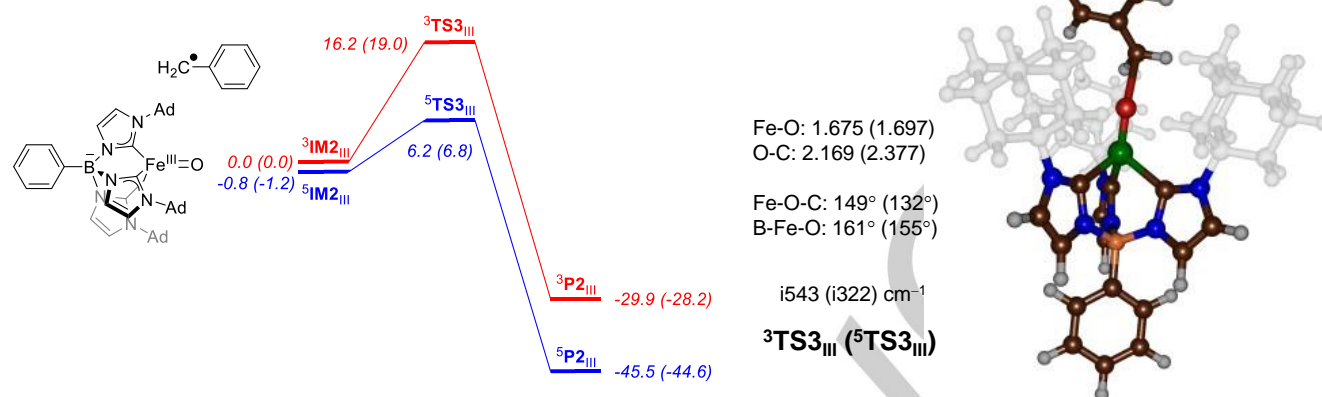
The Fe−O bond is midway between that for the isolated doublet and quartet spin state structures, but the B−Fe−O angle is considerably bent at 158°. Nevertheless, the calculations show spin state equilibration between the doublet and quartet spin state upon formation of the reactant complex. This is in agreement with experimental observation of the formation of an association complex, i.e. reactant complex **Re**. Moreover, the MECP will result in spin-state equilibration between the doublet and quartet spin states.

Next, we investigated the hydrogen atom abstraction step for the iron(III)-oxo complex, which is shown in Figure 3. As can be seen the hydrogen atom abstraction is high in energy, namely $\Delta E+ZPE^{\ddagger}$ = 26.7 kcal mol^{-1} on the doublet spin state surface, while it is $\Delta E+ZPE^{\ddagger}$ = 18.4 kcal mol^{-1} on the quartet spin state. At the free energy level at 298 K the latter converts to a $\Delta G^{\ddagger}$ = 17.4 kcal mol^{-1}. Both of these values ($\Delta H^{\ddagger}$ and $\Delta G^{\ddagger}$) are in excellent agreement with the experimental values reported above. The mechanism; therefore, starts from a doublet spin iron(III)-oxo reactant and through a spin-state-crossing from doublet to quartet during the lifetime of the reactants complex the quartet spin reactants complex is formed. The latter reacts with toluene through H-atom abstraction. The efficiency of the MECP will determine the overall reaction rate and as the MECP is based on the spin state ordering in the reactants there will be no effect of the toluene substrate and hence zeroth-order kinetics in toluene is predicted as indeed observed experimentally. In particular, a low quantum yield in the MECP will make the spin transition slow and consequently is expected to dominate the rate rather than the higher energy barrier for hydrogen atom abstraction. This is in line with previous studies on a manganese(V)-oxo complex with corrolazine ligand in a reaction with *para*-substituted thioanisole substrates, where

a low-energy triplet spin barrier was by-passed due to an inefficient spin-state transfer and MECP resulting in a singlet spin mechanism instead.[17] The rate determining step; therefore, will be the spin state change from doublet to quartet in or around the reactant complex and MECP. The hydrogen atom abstraction will then take place on a quartet spin state surface.

The overall hydrogen atom abstraction barriers are much higher in energy than those reported previously for alternative iron(IV)-oxo species of heme and nonheme oxidants. For example, using the same method and basis set a value of $\Delta E+ZPE$ = 12.1 − 12.4 kcal mol^{-1} was obtained for hydrogen atom abstraction from toluene by a cytochrome P450 Compound I model containing iron(IV)-oxo porphyrin cation radical species with thiolate axial ligand.[18] This model of cytochrome P450 Compound I was a minimal cluster model containing the porphyrin, axial and distal ligands and substrate only and no second-coordination sphere groups, such as protein residues were included. Hence substrate approach in those studies did not encounter stereochemical interactions. Moreover, calculations on a nonheme iron(IV)-oxo enzymatic model with toluene gave a hydrogen atom abstraction barrier of $\Delta E+ZPE$ = 7.6 kcal mol^{-1}.[19] Therefore, structure $\mathbf{1}_{III}$ reacts with a substantially higher barrier as compared to iron(IV)-oxo systems reported before that had no second-coordination sphere perturbations.

To find out if the iron(IV)-oxo species $\mathbf{1}_{IV}^{+}$ also has high energy hydrogen atom abstraction barriers we did calculations on that system as well for comparison. Interestingly, the hydrogen atom abstraction from toluene by $\mathbf{1}_{III}$ is close to thermoneutral on the quartet spin state ($^{4}\mathbf{IM1}_{III}$ is $\Delta E+ZPE$ = 1.3 kcal mol^{-1} above $^{2}\mathbf{Re}_{III}$) but highly endothermic on the doublet spin state at

5

Fe-O: 1.675 (1.697)
O-C: 2.169 (2.377)

Fe-O-C: 149° (132°)
B-Fe-O: 161° (155°)

i543 (i322) cm^{-1}

^{3}**TS3**$_{III}$ (^{5}**TS3**$_{III}$)

Figure 4. Potential energy landscape with ΔE+ZPE (ΔG) values in kcal mol^{-1} as taken from the B3LYP calculations for electrophilic addition of tolyl radical to ^{2,4}**1**$_{III}$. Also shown are optimized geometries of the transition states with bond lengths in angstroms, bond angles in degrees and the imaginary frequency in cm^{-1}. Free energies calculated at 298 K.
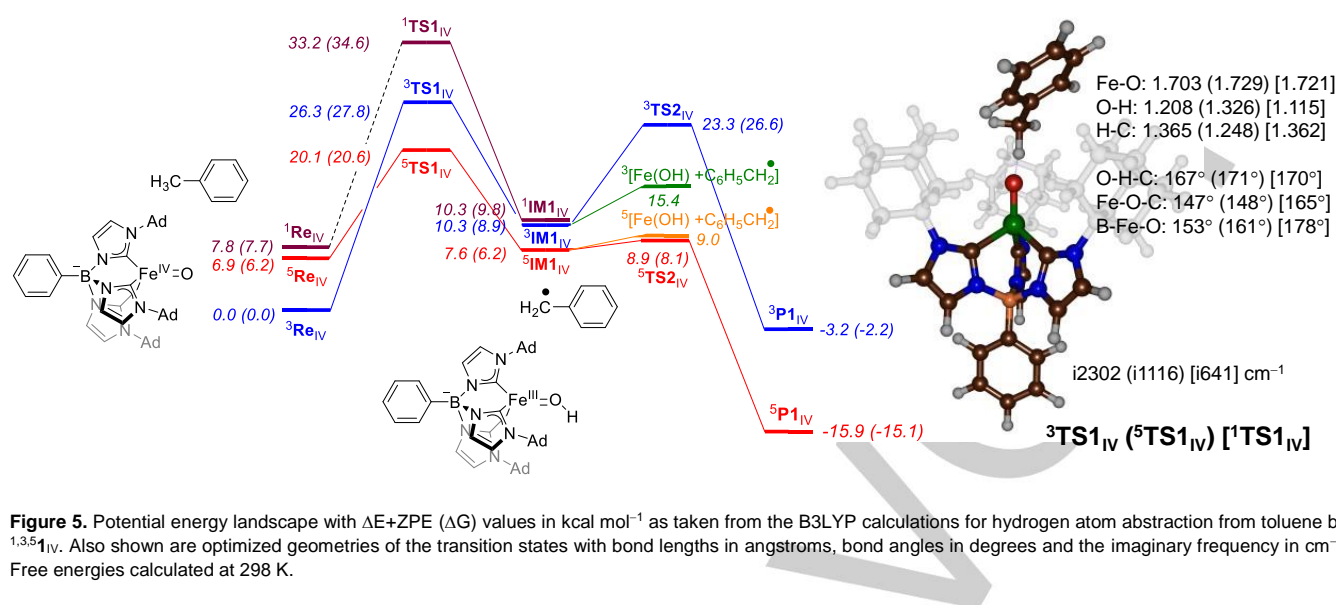
ΔE+ZPE = 18.9 kcal mol^{-1}. The reason the quartet spin transition state is lower in energy than the doublet spin transition state for hydrogen atom abstraction is due to electron transfer from the substrate into the vacant σ^*_{z2} molecular orbital that gives an exchange-enhanced and stabilized radical intermediate ^{4}**IM1**$_{III}$ with four unpaired electrons in 3d-type orbitals coupled to a down-spin electron on the substrate: $\pi^*_{xy}{}^2 \pi^*_{xz}{}^1 \pi^*_{yz}{}^1 \sigma^*_{x2-y2}{}^1 \sigma^*_{z2}{}^1 \phi_{Sub}{}^1$. As such, in the hydrogen atom abstraction a spin state crossing from the doublet to the quartet spin state will take place.

The transition state structures for ^{2,4}**TS1**$_{III}$ are shown on the right in Figure 3. The enthalpy and free energy of activation of the ^{4}**TS1**$_{III}$ structure matches the values from the Eyring plots well. The imaginary frequency for the hydrogen atom abstraction is very high, namely i1985 cm^{-1} for ^{4}**TS1**$_{III}$ and i1235 cm^{-1} for ^{2}**TS1**$_{III}$. The large values of imaginary frequencies indicate narrow and sharp peaks, where the hydrogen transfer will be accompanied with a large amount of quantum mechanical tunneling. These values are typical for hydrogen atom abstraction transition states and similar to those reported previously that generally gave values in the region of i1000 – i1600 cm^{-1}.[20] In particular for P450 Compound I in reaction with toluene the quartet and doublet spin hydrogen atom abstraction barriers had values of i1950 and i1618 cm^{-1}, respectively.[18] The former is close to the one found for ^{4}**TS1**$_{III}$. In both ^{2,4}**TS1**$_{III}$ the hydrogen atom transfer happens late with relatively long C–H distances of 1.594 and 1.387 Å, while the O–H distances are much shorter at 1.088 and 1.175 Å for the doublet and quartet spin states, respectively. The Fe–O bond has considerably elongated to well over 1.7 Å in both transition states as a result of electron transfer from the substrate into a metal-oxo antibonding orbital.

After hydrogen atom abstraction and the formation of radical intermediate **IM1**, we searched for pathways for OH rebound via transition state ^{4,2}**TS2**$_{III}$ to form phenylmethanol products. This pathway; however, requires high barriers on both spin states with a magnitude of ΔE+ZPE‡ = 32.4 kcal mol^{-1} on the quartet spin state and 53.1 kcal mol^{-1} on the doublet spin state. Consequently, OH rebound will be unfeasible for the iron(III)-oxo complex under

room temperature and ambient pressure conditions. Indeed, no evidence of alcohol products was observed experimentally. Either this is the result from the low oxidation state of the metal complex or due to steric restraints of the adamantyl groups that prevent close approach of the tolyl radical and the formation of the C–O bond. To find the origin of the high rebound barrier, we explored a truncated model with the adamantyl groups removed, *vide supra*. Nevertheless, the overall reaction energy for the formation of alcohol products from an iron(III)-oxo and toluene is considerable at ΔE+ZPE = 22.5 kcal mol^{-1}, hence is highly endothermic. Therefore, the overall reaction toluene hydroxylation is thermodynamically challenging for the iron(III)-oxo species.

To test whether the radical and iron(II)-hydroxo species can split and separate into two isolated species, we calculated the energy of isolated radical products and find these to be ΔE+ZPE = 8.4 kcal mol^{-1} in energy above ^{2}**Re**$_{III}$ to give ^{3}FeOH and ^{2}C$_6$H$_5$CH$_2$•. Therefore, the most likely mechanism for the reaction of toluene with the iron(III)-oxo complex ^{2}**1**$_{III}$ is the formation of an iron(II)-hydroxy species and a tolyl radical. In particular, the radical is likely to split off from complex **IM1**$_{III}$ and will not react via OH rebound to form the alcohol product. Instead, the tolyl radical reacts further in solution, for instance, through a subsequent reaction with another iron(III)-oxo species. As the iron(II)-hydroxy species and the C$_6$H$_5$CH$_2$• radical are long-lived, we considered a reaction of C$_6$H$_5$CH$_2$• radical with another iron(III)-oxo species (^{2,4}**1**$_{III}$), see Figure 4. The complexes [PhB(AdIm)$_3$Fe^{III}=O--C$_6$H$_5$CH$_2$•] are designated **IM2** and have been calculated in the overall triplet or quintet spin. The energy landscape for the reaction of a tolyl radical with ^{2,4}**1**$_{III}$ gives low free energy of activation of ΔE+ZPE‡ = 6.2 kcal mol^{-1} on the quintet spin state surface and 16.2 kcal mol^{-1} on the triplet spin state. These barriers are relatively low in energy and should be feasible under room temperature conditions.

Figure 5. Potential energy landscape with ΔE+ZPE (ΔG) values in kcal mol⁻¹ as taken from the B3LYP calculations for hydrogen atom abstraction from toluene by ¹,³,⁵**1**$_{IV}$. Also shown are optimized geometries of the transition states with bond lengths in angstroms, bond angles in degrees and the imaginary frequency in cm⁻¹. Free energies calculated at 298 K.

Moreover, the overall addition reaction is highly exothermic and releases ΔE+ZPE = −29.9 kcal mol⁻¹ to form ³**P2**$_{III}$ and −45.5 kcal mol⁻¹ to form ⁵**P2**$_{III}$. Consequently, when radical is released after hydrogen abstraction it can react with another reactant molecule rapidly and form the coupled product. This step will be highly dependent on the concentration of the iron(III)-oxo complex in the solution.

Optimized transition state structures ³**TS3**$_{III}$ and ⁵**TS3**$_{III}$ are shown on the right-hand-side of Figure 4. They are characterized with a long C−O bond of 2.169 Å in the triplet spin state and 2.377 Å in the quintet spin state. These distances are not unusual and seen before for OH rebound or epoxidation transition states by iron-oxo complexes.[14af,21] In the optimized structures, the Fe−O−C angles are considerably bent, while the B−Fe−O angles have decreased to 161° and 155° for the triplet and quintet spin states, respectively. The imaginary frequency in the **TS3** transition state represents the C−O stretching vibration and has values of i543 and i322 cm⁻¹ for ³**TS3**$_{III}$ and ⁵**TS3**$_{III}$, respectively. Overall, the results presented in Figures 2 and 3 show that the reaction of ²**1**$_{III}$ with toluene is not expected to give alcohol products as normally found for the reaction of a metal-oxo species with toluene. Instead, the calculations find low energy pathways for the formation of iron(II)-hydroxo and iron(II)-benzoxy complexes. The tolyl radical that is released to provide the iron(II)-hydroxo product can react with another molecule of ²**1** in solution. These results are in excellent agreement with experimental observations that reported the same products. Moreover, experimental work[10] reported that the iron(II)-hydroxo and iron(II)-benzoxy complexes are formed in a ratio of 1:0.65, which implicates that approximately two units of iron(III)-oxo are needed to form one unit of iron(II)-benzoxy material, in agreement with the calculated results presented here.

Structure and reactivity of 1$_{IV}$⁺.
To understand why radical rebound does not occur and how a potential iron(IV)-oxo species would react, we did a further set of calculations. Thus, we took the optimized geometry of ²**1**$_{III}$ and ²**Re**$_{III}$ and recalculated them with an overall charge of +1 and odd multiplicity to create the corresponding iron(IV)-oxo species. Subsequently, the reaction mechanism of Scheme 2 was calculated for the iron(IV)-oxo model complex and the energetic landscape is shown in Figure 5. The triplet spin for the iron(IV)-oxo species is the ground state with π*$_{xy}$² π*$_{xz}$¹ π*$_{yz}$¹ configuration, while the quintet spin state with π*$_{xy}$¹ π*$_{xz}$¹ π*$_{yz}$¹ σ*$_{x2-y2}$¹ is higher in energy by ΔE+ZPE = 6.9 kcal mol⁻¹. The singlet spin state was also considered but found to be ΔE+ZPE = 7.8 kcal mol⁻¹ above the triplet ground state. Indeed most previous studies on biomimetic nonheme iron(IV)-oxo species typically found a triplet spin ground state.[14,19,21-23] The only counter-examples to these patterns are a singlet spin ground state for iron(IV)-oxo with a quinisox ligand found by Roithová et al and a quintet spin ground state for a pentacoordinated system of Ray et al.[24] By contrast, to these biomimetic systems are enzymatic nonheme iron(IV)-oxo species that all have been characterized as quintet spin ground states due to differences in coordination environment.[13,25,26] Geometrically, the iron(IV)-oxo distance is 1.600 Å in the triplet spin state, 1.547 Å in the singlet spin state and 1.644 Å in the quintet spin state. These distances match previous calculations and experimental reports on iron(IV)-oxo geometries well and also are close to the ones reported above for the iron(III)-oxo species.[14] As such, reduction of iron(IV)-oxo to iron(III)-oxo is not expected to dramatically alter the Fe−O distance.

Next, the reaction mechanism with toluene was explored and the results are shown in Figure 5. Similarly, for the iron(III)-oxo complex reported above in Figure 3, the iron(IV)-oxo species reacts with a high hydrogen atom abstraction barrier of activation of ΔE+ZPE = 20.1 kcal mol⁻¹ on the quintet spin state surface, 26.3 kcal mol⁻¹ on the triplet spin state surface and 33.2 kcal mol⁻¹ on the singlet spin state. Consequently, both **1**$_{III}$ and **1**$_{IV}$ are sluggish oxidants that are expected to react with toluene slowly. Moreover, it appears that the iron(III)-oxo species is a slightly better oxidant than the corresponding iron(IV)-oxo species under the same conditions with the same substrate as it reacts with lower hydrogen atom abstraction barriers.
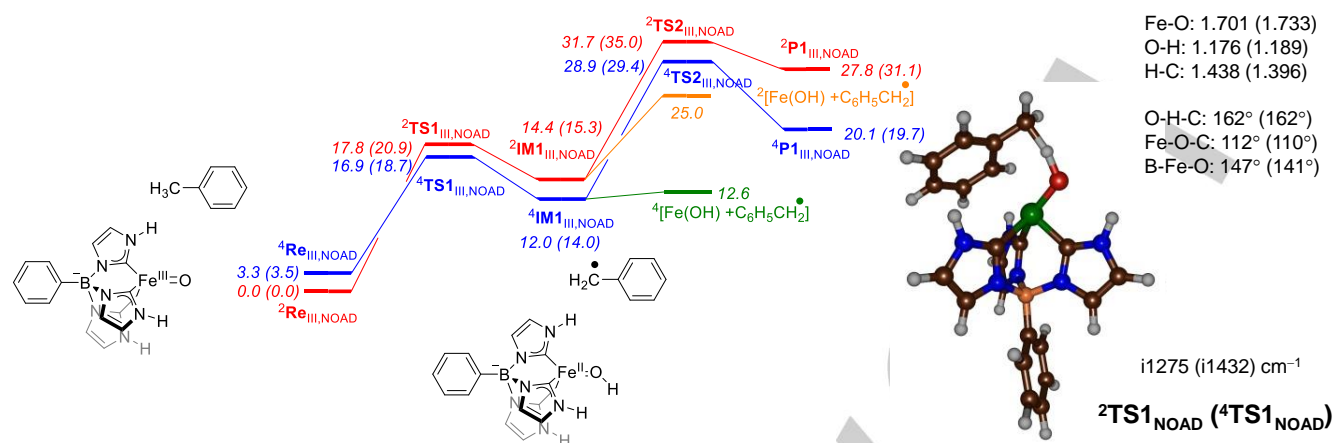
Figure 6. Potential energy landscape with $\Delta E+ZPE$ values in kcal mol^{-1} as taken from the B3LYP calculations for hydrogen atom abstraction from toluene by the truncated model $^{2,4}\mathbf{1}_{NOAD}$. Also shown are optimized geometries of the transition states with bond lengths in angstroms, bond angles in degrees and the imaginary frequency in cm^{-1}.

The optimized geometries of the hydrogen atom abstraction transition states are shown in Figure 5. The hydrogen abstraction barrier $^5\mathbf{TS1}_{IV}$ happens much earlier than that seen for $^4\mathbf{TS1}_{III}$ with shorter C–H and longer O–H distances: The O–H distances are 1.208 and 1.326 Å, while the C–H distances are 1.365 and 1.248 Å for $^3\mathbf{TS1}_{IV}$ and $^5\mathbf{TS1}_{IV}$, respectively. Similar to the other hydrogen atom abstraction transition states they have a large imaginary frequency of >i1000 cm^{-1}. Structurally, the quintet spin transition state has a geometry that resembles the two iron(III)-oxo transition states. The O–H–C angle is close to linearity for the quintet spin state (171°) and the B–Fe–O angle is also large (161°).

After the hydrogen atom abstraction, we find a small OH rebound barrier of $\Delta E+ZPE$ = 1.3 kcal mol^{-1} above $^5\mathbf{IM1}_{IV}$ leading to the hydroxylated toluene products. On the triplet spin surface the rebound barrier is considerably higher in energy at $\Delta E+ZPE$ = 13.0 kcal mol^{-1} above $^3\mathbf{IM1}_{IV}$. However, the overall rebound barrier is lower in energy than the hydrogen atom abstraction barrier. These calculations show that a reaction of $^{3,5}\mathbf{1}_{IV}$ with toluene has a rate-determining hydrogen atom abstraction and lead efficiently leads to hydroxylation products. The radical dissociation energy was also calculated but found to be of similar energy to the OH rebound on the quintet spin state surface. As a result, radical release and OH rebound may be competitive for the iron(IV)-oxo species in reaction with toluene. Therefore, the reaction products of $\mathbf{1}_{III}$ with toluene will be different from those of $\mathbf{1}_{IV}$.

Subsequently, we also calculate the reaction of radical, i.e. $C_6H_5CH_2^{\bullet}$, with another molecule of $^5\mathbf{1}_{IV}^{+}$. A barrier of $\Delta E+ZPE^{\ddagger}$ = 8.8 kcal mol^{-1} on the doublet spin state and $\Delta E+ZPE^{\ddagger}$ = 7.7 kcal mol^{-1} on the quartet spin state for C–O bond formation and a reaction to the benzoxy product is found. Therefore, the benzoxy-formation pathway has similar barriers whether it is from an iron(III) or iron(IV) complex. Moreover, for the iron(IV)-oxo species this makes the benzoxy formation channel higher in energy than OH rebound to form alcohol product complexes. Consequently, the iron(IV)-oxo species will react with toluene through aliphatic

hydroxylation and form phenylmethanol, whereas the iron(III)-oxo species gives iron(II)-hydroxo and benzoxy products instead.

To further confirm that the reaction of $^5\mathbf{1}_{IV}^{+}$ with $C_6H_5CH_2^{\bullet}$ gives benzoxy products via transition state **TS3**, we calculated an intrinsic reaction coordinate (IRC) pathway from the transition state. In particular, we used $^4\mathbf{TS3}_{IV}$ as the starting point of the IRC, and the forward and reverse scans obtained the expected products, namely the benzoxy complex in the forward direction and the iron(IV)-oxo plus radical in reverse direction. The $^4\mathbf{TS3}_{IV}$ energy is at the highest point of the potential energy surface and the geometries of two ends of the curve correspond to that of the reactants/products.

Structure and reactivity of $\mathbf{1}_{NOAD}$.

Recent work has shown that second-coordination sphere effects can influence structure, reactivity and bifurcation pathways.[26] To find out what the effect of the adamantyl groups on structure and reactivity of the iron(III)-oxo complex is, we created a truncated model of $\mathbf{1}_{III}$ with the adamantyl groups replaced by hydrogen atoms (model $\mathbf{1}_{NOAD}$) and recalculated the mechanism of toluene activation through Scheme 2 above. Figure 6 displays the energy landscape for toluene activation by the truncated model without adamantyl groups. The reactant complex is in the doublet spin state, similarly to the model with adamantyl groups, and consequently the truncated model has the same spin state ordering and electronic ground state and orbital configuration. The quartet spin state is higher in energy by $\Delta E+ZPE$ = 3.3 kcal mol^{-1}.

Next the reaction with toluene was explored for the iron(III)-oxo model without adamantyl groups and hydrogen atom abstraction barriers of $\Delta E+ZPE^{\ddagger}$ = 16.9 and 17.8 kcal mol^{-1} on the quartet and doublet spin state surfaces are obtained. Particularly, the doublet spin barrier is considerably lower in energy than that found for model $\mathbf{1}_{III}$. Therefore, second-coordination sphere effects in $\mathbf{1}_{III}$ contribute to a rise in the hydrogen atom free energy of activation on the doublet spin state by almost 10 kcal mol^{-1}.
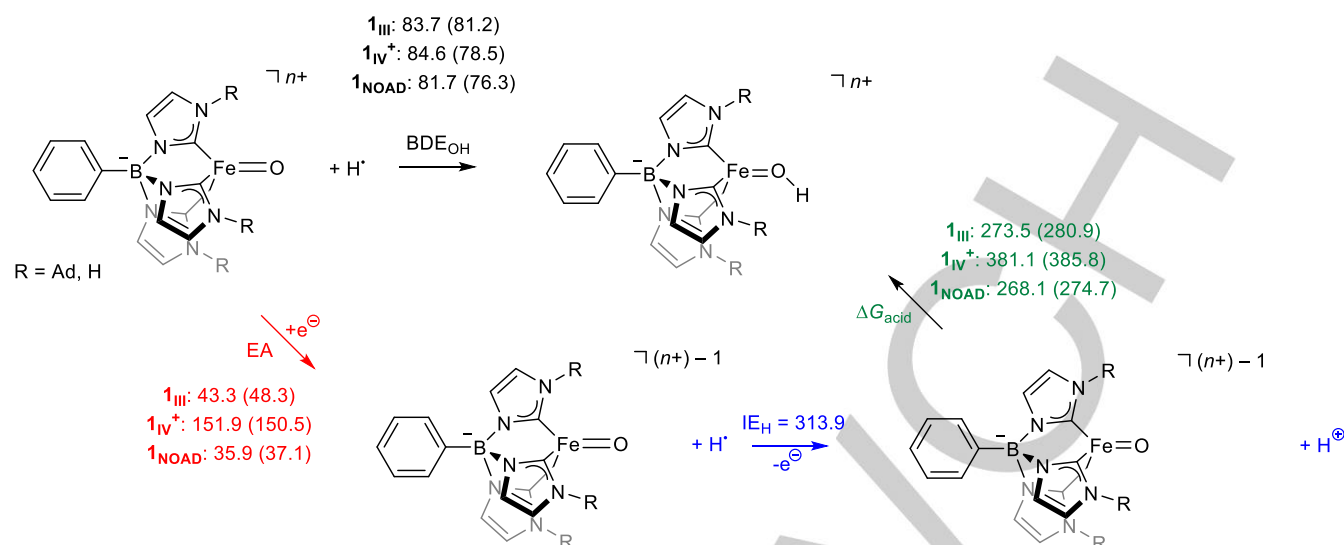
Figure 7. Thermodynamic reaction cycle for iron(III)-oxo and iron(IV)-oxo complexes. Values (kcal mol⁻¹) are given as UB3LYP/BS2//UB3LYP/BS1 energies with zero-point corrections out of parenthesis and free energy changes in parenthesis.

By contrast, on the quartet spin barrier show little effect of the second coordination sphere. Most probably this is the result from differences in electron transfer on the doublet and quartet spin state as well as substrate approach being lesser influenced along the Fe–O axis. Thus, in the quartet spin state an electron transfer takes place into the σ^*_{z2} orbital that is located along the Fe–O bond and consequently attack along this coordinate by the substrate results in minimal interactions with the adamantyl groups. On the other hand, on the doublet spin state an electron transfer into the π^*_{yz} orbital takes place and the substrate cannot correctly orient for the electron transfer into that orbital due to the steric constraints of the adamantyl groups.

The optimized transition state structures of ^{2,4}**TS1**$_{NOAD}$ are shown on the right-hand-side of Figure 5. Both doublet and quartet spin transition states have the oxo group considerably bent with respect to the B–Fe axis by 147 and 141°. In addition, there is major bending in the Fe–O–C angle with values of 112 and 110° in the doublet and quartet spin states. Both B–Fe–O and Fe–O–C angles are, therefore, dramatically different from those found for the reaction of **1**$_{III}$ with toluene. Consequently, the adamantyl group pushes the substrate into an attack along the Fe–O axis even though sideways approach is energetically favored. Despite the differences in orientation, the C–H and O–H optimized distances in the transition state structures for ^{2,4}**TS1**$_{NOAD}$ are close to those found for ^{2,4}**TS1**$_{III}$.

Following formation of the radical intermediate, two reaction channels were explored, namely radical release and OH rebound. For the truncated model, the radical release energies are very similar to those from **1**$_{III}$ above with an overall endothermicity of ΔE+ZPE = 12.6 kcal mol⁻¹ on the quartet spin state and ΔE+ZPE = 25.0 kcal mol⁻¹ on the doublet spin state. On both spin state surfaces for the truncated model, the OH rebound barriers are high in energy with magnitude of ΔE+ZPE = 28.9 kcal mol⁻¹ on the quartet spin state and ΔE+ZPE = 31.7 kcal mol⁻¹ on the doublet spin state with respect to ^{2}**Re**$_{III,NOAD}$. As such, the adamantyl substituents are not responsible for the lack of OH rebound and the fact that substrate hydroxylation does not occur.

Instead, it appears the iron(III)-oxo can only react in one-electron transfer catalytic processes due to the formation of a low and unreactive oxidation state. Thus, a substrate hydroxylation will reduce the iron(III)-oxo to an iron(I) product, which appears to be thermodynamically disfavored.

In summary, the adamantyl substituents of the oxidant slow down the hydrogen atom abstraction step for toluene activation, but do not change the reaction mechanism and product distribution. Moreover, the iron(III)-oxo group appears to have limited oxidative power and is unable to react through aliphatic and aromatic hydroxylation, epoxidation or sulfoxidation. As such, enzymatic systems, like nonheme iron enzymes, will create an iron(IV)-oxo species in their catalytic cycle to catalyze challenging C–H activation reactions in nature. We will analyze the reasons of the differences between iron(III)-oxo and iron(IV)-oxo in the next section.

Thermodynamic properties of 1$_{III}$ versus 1$_{IV}^+$.

To find out whether the reactivity and selectivity differences of **1**$_{III}$ and **1**$_{IV}^+$ with toluene are based on the thermodynamic properties of these complexes, we calculated a thermochemical reaction cycle, see Figure 7. This cycle contains the electron affinity of the oxidant and the acidity of the iron-hydroxo complexes. In particular, the top reaction investigates the strength of the O–H bond in the iron(II)-hydroxo and iron(III)-hydroxo species that are formed upon hydrogen atom abstraction from a substrate by the iron(III)-oxo and iron(IV)-oxo oxidants, respectively. The O–H bond dissociation (free) energy (BDE$_{OH}$) is calculated from isolated species at the UB3LYP/BS2//UB3LYP/BS1+ZPE level of theory. Values of ΔE+ZPE = 83.7 and 84.6 kcal mol⁻¹ for the BDE$_{OH}$ corresponding to the iron(III)-oxo and iron(IV)-oxo species are found. The two BDE$_{OH}$ values for **1**$_{III}$ and **1**$_{IV}^+$ are very close in energy and imply that the two oxidants should react with similar hydrogen atom abstraction barriers.

9
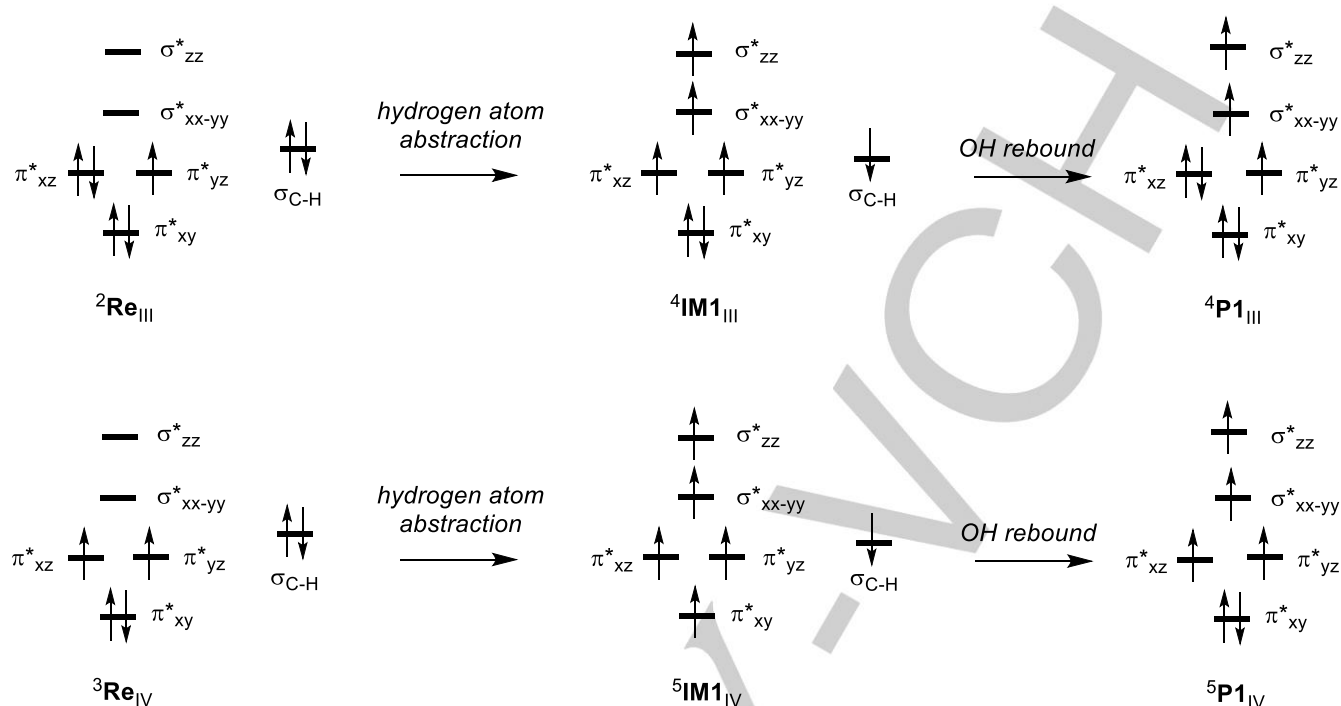
Figure 8. Electron configuration changes for toluene hydroxylation by an iron(III)-oxo species (top) and iron(IV)-oxo species (bottom).

Indeed the two lowest energy hydrogen atom abstraction free energy of activation are $\Delta E+ZPE^{\ddagger}$ = 18.4 and 20.1 kcal mol^{-1} for the reaction of toluene with $\mathbf{1}_{III}$ and $\mathbf{1}_{IV}^{+}$, respectively.

Thermodynamically, the energy for the reaction step from the reactant complexes **Re** to form **IM1** should be equal to the difference of the C−H bond of toluene that is broken minus the O−H of the iron-hydroxo species that is formed. We calculate a BDE_{CH} for toluene of $\Delta E+ZPE$ = 85.9 kcal mol^{-1}. Consequently, the difference between BDE_{CH} and BDE_{OH} is +2.2 kcal mol^{-1} for the reaction with $\mathbf{1}_{III}$, while it is 1.3 kcal mol^{-1} for the reaction with $\mathbf{1}_{IV}^{+}$. These values are close in energy to the difference in energy between low-spin reactant complexes and high-spin radical intermediates **IM1**. As such, the energy landscape follows the calculated thermodynamics of the reaction. We also calculated the BDE_{OH} of the complex with adamantyl groups removed and find a value of $\Delta E+ZPE$ = 81.7 kcal mol^{-1} its corresponding iron(III)-oxo system. This BDE value is close to the one found for $\mathbf{1}_{III}$ and therefore the BDE_{OH} appears to be largely unaffected by the second coordination sphere of the oxidant. Moreover, the adamantyl groups do not contribute electron density toward the metal-oxo group. As such, the same thermodynamics should be expected for $\mathbf{1}_{III}$ and $\mathbf{1}_{NOAD}$. Although the hydrogen atom abstraction energy is more endothermic for the $\mathbf{1}_{NOAD}$ system, the radical dissociation is similar in support of similar BDE values. Despite similarities in BDE_{OH} value, of course, the kinetics are dramatically affected by the second-coordination sphere. In principle, the BDE_{OH} values are made up from an electron transfer and a proton transfer, which may have different effects on the chemical system. We, therefore, also calculated the electron affinity of the oxidants (EA) and the gas-phase acidity (ΔG_{acid}) of

the iron-hydroxo species as shown from the reactions in Figure 6. The ionization energy of a hydrogen atom was taken from experimental data from the literature.[27] As can be seen from Figure 6, the iron(IV)-oxo species has a large electron affinity and consequently a highly stable reduced species is formed. This is less so for the iron(III)-oxo species. Moreover, a drop in electron affinity for the iron(III)-oxo species leads to a drop in gas-phase acidity to balance the overall similar BDE values.

Electron-transfer processes during toluene hydroxylation.
To understand, why the iron(III)-oxo reacts with high barriers for OH rebound, while they are much lower for the iron(IV)-oxo species, we analyzed the electron transfer processes for the substrate hydroxylation reactions. Thus, $\mathbf{1}_{III}$ is in a doublet spin state with orbital configuration $\pi^{*}_{xy}{}^{2} \pi^{*}_{xz}{}^{2} \pi^{*}_{yz}{}^{1}$. Upon hydrogen atom abstraction from toluene, the metal changes oxidation state from iron(III) to iron(II) and transfers to a high-spin state with a quintet spin iron(II)-hydroxo coupled to a toluene radical and overall configuration: $\pi^{*}_{xy}{}^{2} \pi^{*}_{xz}{}^{1} \pi^{*}_{yz}{}^{1} \sigma^{*}_{x2-y2}{}^{1} \sigma^{*}_{z2}{}^{1}$. During the OH rebound a second electron is transferred into the metal center, which is reduced to iron(I) which has the electronic configuration $\pi^{*}_{xy}{}^{2} \pi^{*}_{xz}{}^{2} \pi^{*}_{yz}{}^{1} \sigma^{*}_{x2-y2}{}^{1} \sigma^{*}_{z2}{}^{1}$. As the iron(II)-hydroxo has a low electron affinity, the iron(I) state is difficult to form and consequently the OH rebound is hampered and benzyl radical release is triggered instead. Indeed, when we calculate the electron affinity of the iron(II)-hydroxo species, we find a very low value of less than 10 kcal mol^{-1}, which implies that little energy will be released upon its reduction. This is very different for the iron(IV)-oxo species that forms iron(III)-hydroxo after hydrogen atom abstraction. The latter has a much higher electron affinity

10

than the iron(II)-hydroxo and consequently can easily take up another electron and assist in a two-electron transfer reaction with substrate.

For the iron(IV)-oxo species the reactant is in a triplet spin state with configuration $\pi^*_{xy}{}^2 \pi^*_{xz}{}^1 \pi^*_{yz}{}^1$. Hydrogen atom abstraction results in a spin-crossover to the quintet spin state with the full metal 3d-block exchange stabilized. Subsequently, OH rebound results in an iron(II) product state with electronic configuration $\pi^*_{xy}{}^2 \pi^*_{xz}{}^1 \pi^*_{yz}{}^1 \sigma^*_{x2-y2}{}^1 \sigma^*_{z2}{}^1$. The second electron transfer for the latter step is energetically favorable and consequently the iron(IV)-oxo species is able to catalyze reactions with substrate through substrate hydroxylation, sulfoxidation and epoxidation reactions, whereas the iron(III)-oxo will not be able to perform those reactions.

Conclusion

In this work a combined experimental and computational study is presented on a biomimetic model with central iron(III)-oxo group. Rate-constants measurements show zeroth-order kinetics in toluene and no kinetic isotope effect for the replacement of hydrogen by deuterium. To understand the product distributions and the observed kinetics, a computational study was performed. Our calculations are validated against experimentally reported spectroscopic and crystallographic parameters and good agreement is found. In particular, the calculated energetics match the enthalpy and free energy of activation from the Eyring plots excellently and structural parameters of the reactant complexes are in good agreement with crystallography and infrared spectroscopy features. Although the doublet spin iron(III)-oxo is well separated from the quartet spin state in the gas-phase, upon substrate approach the spin state gap narrows and possible equilibration and spin change occurs. We then study the reaction with toluene and although a facile hydrogen atom abstraction can take place the subsequent OH rebound barrier for toluene hydroxylation is high in energy and unfeasible under ambient conditions. Therefore, the iron(III)-oxo forms an iron(II)-hydroxo with concomitant release of a tolyl radical that dissipates back into the solution, where it can react with another iron(III)-oxo species to form a benzoxy complex. To understand the reactivity patterns, we repeated the calculations with an iron(IV)-oxo species. Interestingly, the hydrogen atom abstraction barrier is higher in energy than the one found for the iron(III)-oxo species. However, the iron(III)-hydroxo intermediate reacts with tolyl radical via a low energy barrier leading to hydroxytoluene products. The alternative radical release was also tested but the barriers for benzoxy formation are considerably higher in energy than those for OH rebound. As such the iron(IV)-oxo species will react with toluene to give different products than the iron(III)-oxo species. Finally, a truncated model was investigated to find out whether the differences in reactivity are due to the second coordination sphere of the oxidant. Although the hydrogen atom abstraction barriers are somewhat lower in energy, the OH rebound is still substantial. An analysis of the thermochemical properties of the various complexes shows that the iron(IV)-oxo species is a versatile oxidant, whereas the iron(III)-oxo has limited catalytic possibilities. Therefore, the corresponding iron(IV)-oxo and iron(III)-oxo species react differently due to their oxidation state and electron affinity differences.

Experimental Section

Experiment.

General Considerations

All manipulations involving air- or moisture sensitive compounds and their preparation were performed under an inert atmosphere of dry N_2 by standard Schlenk techniques or in an M. Braun glovebox. Glassware used was oven dried for at least 12 h at 140 °C before use. All solvents were purchased from Sigma-Aldrich and used after being dried using a Glass Contour solvent purification system. The iron(III)-oxo complex [PhB(AdIm)$_3$FeO] ($\mathbf{1}_{III}$) was prepared and purified according to the literature [10] and stored in the solid state at -35 °C until use.

Kinetics studies

Kinetics data were using UV-visible spectroscopy collected using an Agilent Technologies Cary 60 UV-visible spectrometer connected to a Unisoku thermostat. All kinetics data was obtained in THF solutions. The rates of reaction were obtained by measuring the disappearance of the band at 525 nm and fit to an exponential decay. The activation parameters for the reaction were obtained from the temperature dependence of the rate constants.

Computation.

All computational work was performed using the Gaussian-09 software package,[28] and utilized density functional theory methods. The initial starting point was taken from the crystal structure coordinates reported previously.[10] Geometry optimizations, analytical frequencies, geometry scans and intrinsic reaction coordinate scans were performed with a modest def2-SVP basis set on all atoms (basis set BS1).[29] Single point calculations were performed using the def2-TZVP basis set: basis set BS2. All calculations include a continuum polarized conductor model with a dielectric constant mimicking toluene.[30] We tested various density functional theory methods, namely B3LYP,[31] BP86,[32] B3LYP-D3,[31,33] and PBE0.[34] Spectroscopic parameters of the isolated iron(III)-oxo complexes and minimum energy crossing points (MECP) were calculated in Orca.[35] Vibrational frequencies were unscaled values taken from the frequency calculations. ^{57}Fe Mössbauer parameters were calculated as before,[36] using ORCA5.0 to obtain the isomer shift of ^{57}Fe by calculating its electron density. Free energies were calculated at 298 K and contain, thermal, entropic, solvent and zero-point corrections.

[1]   a) P. R. Ortiz de Montellano (Ed.) Cytochrome P450: Structure, Mechanism and Biochemistry. 3rd ed., Kluwer Academic/Plenum Publishers, New York, 2004; b) I. G. Denisov, T. M. Makris, S. G. Sligar, I. Schlichting, *Chem. Rev.* **2005**, *105*, 2253–2277; c) B. Meunier, S. P. de Visser, S. Shaik, *Chem. Rev.* **2004**, *104*, 3947–3980; d) K. M. Kadish, K. M. Smith and R. Guilard (Eds.) Handbook of Porphyrin Science. World Scientific: New Jersey, 2010; e) X. Huang, J. T. Groves, *Chem. Rev.* **2018**, *118*, 2491–2553; f) N. P. Dunham, F. Arnold, *ACS Catal.* **2020**, *10*, 12239–12255.

[2] a) E. I. Solomon, T. C. Brunold, M. I. Davis, J. N. Kemsley, S. K. Lee, N. Lehnert, F. Neese, A. J. Skulan, Y. S. Yang, J. Zhou, *Chem. Rev.* **2000**, *100*, 235–349; b) T. D. H. Bugg, *Curr. Opin. Chem. Biol.* **2001**, *5*, 550–555; c) S. P. de Visser, D. Kumar (Eds.) Iron-containing enzymes: Versatile catalysts of hydroxylation reactions in nature, Royal Society of Chemistry Publishing, Cambridge (UK), 2011; d) A. Salminen, A. Kauppinen, K. Kaarniranta, *Cell. Mol. Life Sci.* **2015**, *72*, 3897–3914.

[3] a) M. J. Ryle, R. P. Hausinger, *Curr. Opin. Chem. Biol.* **2002**, *6*, 193–201; b) C. Krebs, D. G. Fujimori, C. T. Walsh, J. M. Bollinger Jr, *Acc. Chem. Res.* **2007**, *40*, 484–492; c) S. P. de Visser, G. Mukherjee, H. S. Ali, C. V. Sastri, *Acc. Chem. Res.* **2022**, *55*, 65–74.

[4] a) J. C. Price, E. W. Barr, B. Tirupati, J. M. Bollinger Jr, C. Krebs, *Biochemistry* **2003**, *42*, 7497–7508; b) D. A. Proshlyakov, T. F. Henshaw, G. R. Monterosso, M. J. Ryle, R. P. Hausinger, *J. Am. Chem. Soc.* **2004**, *126*, 1022–1024.

[5] a) J. M. Bollinger Jr, J. C. Price, L. M. Hoffart, E. W. Barr, C. Krebs, *Eur. J. Inorg. Chem.* **2005**, *21*, 4245–4254; b) E. G. Kovaleva, J. D. Lipscomb, *Nat. Chem. Biol.* **2008**, *4*, 186–193; c) K. Gorres, R. T. Raines, *Crit. Rev. Biochem. Mol. Biol.* **2010**, *45*, 106–124; d) M. D. White, E. Flashman, *Curr. Opin. Chem. Biol.* **2016**, *31*, 126–135; e) A. J. Mitchell, N. P. Dunham, R. J. Martinie, J. A. Bergman, C. J. Pollock, K. Hu, B. D. Allen, W.-c. Chang, A. Silakov, J. M. Bollinger Jr, C. Krebs, A. K. Boal, *J. Am. Chem. Soc.* **2017**, *139*, 13830–13836; f) N. P. Dunham, A. J. Mitchell, J. M. Del Río Pantoja, C. Krebs, J. M. Bollinger Jr, A. K. Boal, *Biochemistry* **2018**, *57*, 6479–6488.

[6] a) M. Costas, M. P. Mehn, M. P. Jensen, L. Que Jr., *Chem. Rev.* **2004**, *104*, 939–986; b) M. M. Abu-Omar, A. Loaiza, N. Hontzeas, *Chem. Rev.* **2005**, *105*, 2227–2252; c) P. C. A. Bruijnincx, G. van Koten, R. J. M. Klein Gebbink, *Chem. Soc. Rev.* **2008**, *37*, 2716–2744; d) P. Comba, M. Kerscher, *Coord. Chem. Rev.* **2009**, *253*, 564–574; e) A. R. McDonald, L. Que Jr, *Coord. Chem. Rev.* **2013**, *257*, 414–428; f) W. Nam, Y.-M. Lee, S. Fukuzumi, *Acc. Chem. Res.* **2014**, *47*, 1146–1154; g) K. Ray, F. F. Pfaff, B. Wang, W. Nam, *J. Am. Chem. Soc.* **2014**, *136*, 13942–13958; h) G. Mukherjee, J. K. Satpathy, U. K. Bagha, M. Q. E. Mubarak, C. V. Sastri, S. P. de Visser, *ACS Catal.* **2021**, *11*, 9761–9797.

[7] See, e.g., a) W. Nam, Y.-M. Lee, S. Fukuzumi, *Acc. Chem. Res.* **2018**, *51*, 2014–2022; b) L. Vicens, G. Olivo, M. Costas, *ACS Catal.* **2020**, *10*, 8611–8631; c) V. F. Oswald, J. L. Lee, S. Biswas, A. C. Weitz, K. Mittra, R. Fan, J. Li, J. Zhao, M. Y. Hu, E. E. Alp, E. L. Bominaar, Y. Guo, M. T. Green, M. P. Hendrich, A. S. Borovik, *J. Am. Chem. Soc.* **2020**, *142*, 11804–11817; d) A. L. Robinson, J.-N. Rebilly, R. Guillot, C. Herrero, H. Maisonneuve, F. Banse, *Chem. Eur. J.* **2022**, *28*, e202200217; e) K. Bleher, P. Comba, D. Faltermeier, A. Gupta, M. Kerscher, S. Krieg, B. Martin, G. Velmurugan, S. Yang, *Chem. Eur. J.* **2022**, *28*, e202103452; f) V. Dantignana, J. Serrano-Plana, A. Draksharapu, C. Magallón, S. Banerjee, R. Fan, I. Gamba, Y. Guo, L. Que Jr, M. Costas, A. Company, *J. Am. Chem. Soc.* **2019**, *141*, 15078–15091; g) M. A. Dedushko, M. B. Greiner, A. N. Downing, M. Coggins, J. A. Kovacs, *J. Am. Chem. Soc.* **2022**, *144*, 8515–8528; h) S. Bhattacharya, R. Singh, T. K. Paine, *Chem. Asian J.* **2020**, *15*, 1360–1368; i) Y. Sheng, C. S. Abelson, J. Prakash, A. Draksharapu, V. G. Young Jr, L. Que Jr, *Angew. Chem. Int. Ed.* **2021**, *60*, 20991–20998; j) R. Kumar, B. Pandey, A. Sen, M. Ansari, S. Sharma, G. Rajaraman, *Coord. Chem. Rev.* **2020**, *419*, 213397.

[8] a) C. E. MacBeth, A. P. Golombek, V. G. Young Jr, C. Yang, K. Kuczera, M. P. Hendrich, A. S. Borovik, *Science* **2000**, *289*, 938–941; b) C. J. Reed, T. Agapie, *J. Am. Chem. Soc.* **2019**, *141*, 9479–9484; c) E. M. Matson, Y. J. Park, A. R. Fout, *J. Am. Chem. Soc.* **2014**, *136*, 17398–17401.

[9] E. Andris, R. Navrátil, J. Jašík, M. Puri, M. Costas, L. Que Jr, J. Roithová, *J. Am. Chem. Soc.* **2018**, *140*, 14391–14400.

[10] J. A. Valdez-Moreira, D. M. Beagan, H. Yang, J. Telser, B. M. Hoffman, M. Pink, V. Carta, J. M. Smith, *ACS Cent. Sci.* **2021**, *7*, 1751–1755.

[11] I. Garcia-Bosch, A. Company, C. W. Cady, S. Styring, W. R. Browne, X. Ribas, M. Costas, *Angew. Chem. Int. Ed.* **2011**, *50*, 5648–5653.

[12] R. B. Jordan (ed.), Reaction Mechanisms of Inorganic and Organometallic Systems, 3rd ed.. Oxford University Press, Oxford, 2007.

[13] a) T. Borowski, A. Bassan, P. E. M. Siegbahn, *Chem. Eur. J.* **2004**, *10*, 1031–1041; b) S. P. de Visser, *J. Am. Chem. Soc.* **2006**, *128*, 9813–9824; c) A. V. Nemukhin, I. A. Topol, R. E. Cachau, S. K. Burt, *Theor. Chem. Acc.* **2006**, *115*, 348–353; d) S. Sinnecker, N. Svensen, E. W. Barr, S. Ye, J. M. Bollinger Jr, F. Neese, C. Krebs, *J. Am. Chem. Soc.* **2007**, *129*, 6168–6179; e) E. Godfrey, C. S. Porro, S. P. de Visser, *J. Phys. Chem. A* **2008**, *112*, 2464–2468; f) H. Chen, W. Lai, J. Yao, S. Shaik, *J. Chem. Theory Comput.* **2011**, *7*, 3049–3053; g) E. A. C. Bushnell, G. B. Fortowsky, J. W. Gauld, *Inorg. Chem.* **2012**, *51*, 13351–13356; h) H. J. Kulik, C. L. Drennan, *J. Biol. Chem.* **2013**, *288*, 11233–11241; i) A. Wójcik, M. Radoń, T. Borowski, *J. Phys. Chem. A* **2016**, *120*, 1261–1274; j) S. Álvarez-Barcia, J. Kästner, *J. Phys. Chem. B* **2017**, *121*, 5347–5354; k) A. Timmins, M. Saint-André, S. P. de Visser, *J. Am. Chem. Soc.* **2017**, *139*, 9855–9866; l) R. N. Manna, T. Malakar, B. Jana, A. Paul, *ACS Catal.* **2018**, *8*, 10043–10050; m) J. E. M. N. Klein, G. Knizia, *Angew. Chem. Int. Ed.* **2018**, *57*, 11913–11917; n) J. Xue, J. Lu, W. Lai, *Phys. Chem. Chem. Phys.* **2019**, *21*, 9957–9968; o) S. S. Chaturvedi, R. Ramanan, N. Lehnert, C. J. Schofield, T. G. Karabencheva-Christova, C. Z. Christov, *ACS Catal.* **2020**, *10*, 1195–1209; p) H. S. Ali, R. H. Henchman, J. Warwicker, S. P. de Visser, *J. Phys. Chem. A* **2021**, *125*, 1720–1737; q) C.-C. G. Yeh, S. Ghafoor, J. K. Satpathy, T. Mokkawes, C. V. Sastri, S. P. de Visser, *ACS Catal.* **2022**, *12*, 3923–3937; r) H. S. Ali, S. P. de Visser, *Chem. Eur. J.* **2022**, *28*, e202104167.

[14] a) D. Kumar, H. Hirao, L. Que Jr., S. Shaik, *J. Am. Chem. Soc.* **2005**, *127*, 8026–8027; b) H. Hirao, D. Kumar, L. Que Jr., S. Shaik, *J. Am. Chem. Soc.* **2006**, *128*, 8590–8606; c) S. P. de Visser, *Angew. Chem. Int. Ed.* **2006**, *45*, 1790–1793; *Angew. Chem.* **2006**, *118*, 1822–1825; d) L. Bernasconi, E.-J. Baerends, *Eur. J. Inorg. Chem.* **2008**, 1672–1681; e) A. Dey, *J. Am. Chem. Soc.* **2010**, *132*, 13892–13901; f) H. Hirao, F. Li, L. Que Jr, K. Morokuma, *Inorg. Chem.* **2011**, *50*, 6637–6648; g) S. D. Wong, C. B. Bell III, L. V. Liu, Y. Kwak, J. England, E. E. Alp, J. Zhao, L. Que Jr., E. I. Solomon, *Angew. Chem. Int. Ed.* **2011**, *50*, 3215–3218; h) S. F. Ye, F. Neese, *Proc. Natl. Acad. Sci. USA,* **2011**, *108*, 1228–1233; i) A. Ansari, A. Kaushik, G. Rajaraman, *J. Am. Chem. Soc.* **2013**, *135*, 4235–4249; j) L. Bernasconi, E.-J. Baerends, *J. Am. Chem. Soc.* **2013**, *135*, 8857–8867; k) Y. Liu, X. Guan, E. L.-M. Wong, P. Liu, J.-S. Huang, C.-M. Che, *J. Am. Chem. Soc.* **2013**, *135*, 7194–7204; l) D. Usharani, D. C. Lacy, A. S. Borovik, S. Shaik, *J. Am. Chem. Soc.* **2013**, *135*, 17090–17104; m) S. Stepanović, L. Andjelković, M. Zlatar, K. Andjelković, M. Gruden-Pavlović, M. Swart, *Inorg. Chem.* **2013**, *52*, 13415–13423; n) S. Sahu, M. G. Quesne, C. G. Davies, M. Dürr, I. Ivanović-Burmazović, M. A. Siegler, G. N. L. Jameson, S. P. de Visser, D. P. Goldberg, *J. Am. Chem. Soc.* **2014**, *136*, 13542–13545; o) A. S. Faponle, M. G. Quesne, C. V. Sastri, F. Banse, S. P. de Visser, *Chem. Eur. J.* **2015**, *21*, 1221–1236.

[15] a) N. Taku, A. Noriko, K. Shiori, K. Hiroko, D. David, *Bull. Chem. Soc. Jpn.* **1996**, *69*, 3513–3521; b) A. Raba, M. Cokoja, W. A. Herrmann, F. E. Kühn, *Chem. Commun.* **2014**, *50*, 11454–11458; c) R. A. Baglia, J. P. T. Zaragoza, D. P. Goldberg, *Chem. Rev.* **2017**, *117*, 13320–13352; d) S. Pattanayak, F. G. Cantú Reinhard, A. Rana, S. S. Gupta, S. P. de Visser, *Chem. Eur. J.* **2019**, *25*, 8092–8104.

[16] a) F. Ogliaro, N. Harris, S. Cohen, M. Filatov, S. P. de Visser, S. Shaik, *J. Am. Chem. Soc.* **2000**, *122*, 8977–8989; b) T. Kamachi, K. Yoshizawa, *J. Am. Chem. Soc.* **2003**, *125*, 4652–4661; c) S. Shaik, W. Lai, H. Chen, Y. Wang, *Acc. Chem. Res.* **2010**, *43*, 1154–1165; d) H. Hirao, P. Chuanprasit, Y. Y. Cheong, X. Wang, *Chem. Eur. J.* **2013**, *19*, 7361–7369.

[17] T. Yang, M. G. Quesne, H. M. Neu, F. G. Cantú Reinhard, D. P. Goldberg, S. P. de Visser, *J. Am. Chem. Soc.* **2016**, *138*, 12375–12386.

[18] a) C. Hazan, D. Kumar, S. P. de Visser, S. Shaik, *Eur. J. Inorg. Chem.* **2007**, *2007*, 2966–2974; b) S. Shaik, D. Kumar, S. P. de Visser, *J. Am. Chem. Soc.* **2008**, *130*, 10128–10140.

[19] R. Latifi, M. Bagherzadeh, S. P. de Visser, *Chem. Eur. J.* **2009**, *15*, 6651–6662.

[20] a) D. Kumar, L. Tahsini, S. P. de Visser, H. Y. Kang, S. J. Kim, W. Nam, *J. Phys. Chem. A* **2009**, *113*, 11713–11722; b) P. Barman, P. Upadhyay, A. S. Faponle, J. Kumar, S. S. Nag, D. Kumar, C. V. Sastri, S. P. de Visser, *Angew. Chem. Int. Ed.* **2016**, *55*, 11091–11095; c) A. Timmins, M. G. Quesne, T. Borowski, S. P. de Visser, *ACS Catal.* **2018**, *8*, 8685–8698.

[21] a) S. Ghafoor, A. Mansha, S. P. de Visser, *J. Am. Chem. Soc.* **2019**, *141*, 20278–20292; b) R. Latifi, J. L. Minnick, M. G. Quesne, S. P. de Visser, L. Tahsini, *Dalton Trans.* **2020**, *49*, 4266–42; c) E. F. Gérard, V. Yadav,

D. P. Goldberg, S. P. de Visser, *J. Am. Chem. Soc.* **2022**, *144*, 10752–10767.

[22]   G. Mukherjee, A. Alili, P. Barman, D. Kumar, C. V. Sastri, S. P. de Visser, *Chem. Eur. J.* **2019**, *25*, 5086–5098.

[23]   K. Warm, A. Paskin, U. Kuhlmann, E. Bill, M. Swart, M. Haumann, H. Dau, P. Hildebrandt, K. Ray, *Angew. Chem. Int. Ed.* **2021**, *60*, 6752–6756.

[24]   a) E. Andris, K. Segers, J. Mehara, L. Rulíšek, and J. Roithová, *Angew. Chem. Int. Ed.* **2020**, *59*, 23137–23144; b) K. Warm, A. Paskin, U. Kuhlman, E. Bill, M. Swart, M. Haumann, H. Dau, P. Hildebrandt, K. Ray, *Angew. Chem. Int. Ed.* **2021**, *60*, 6752–6756.

[25]   R. Latifi, M. A. Sainna, E. V. Rybak-Akimova, S. P. de Visser, *Chem. Eur. J.* **2013**, *19*, 4058–4068.

[26]   a) S. Sahu, L. R. Widger, M. G. Quesne, S. P. de Visser, H. Matsumura, P. Moënne-Loccoz, M. A. Siegler, D. P. Goldberg, *J. Am. Chem. Soc.* **2013**, *135*, 10590–10593; b) S. P. de Visser, Y.-T. Lin, H. S. Ali, U. K. Bagha, G. Mukherjee, C. V. Sastri, *Coord. Chem. Rev.* **2021**, *439*, 213914; c) C.-C. G. Yeh, T. Mokkawes, J. M. Bradley, N. E. Le Brun, S. P. de Visser, *ChemBioChem.* **2022**, *2022*, e202200257.

[27]   E. P. Hunter, S. G. Lias, in *NIST Chemistry Webbook*, P. J. Linstrom, W. G. Mallard (Eds), NIST Standard Reference Database, Number 69; National Institute of Standards and Technology: Gaithersburg MD, 20899, http://webbook.nist.gov.

[28]   *Gaussian*-09, Revision D.01, M. J. Frisch, G. W. Trucks, H. B. Schlegel, G. E. Scuseria, M. A. Robb, J. R. Cheeseman, G. Scalmani, V. Barone, B. Mennucci, G. A. Petersson, H. Nakatsuji, M. Caricato, X. Li, H. P. Hratchian, A. F. Izmaylov, J. Bloino, G. Zheng, J. L. Sonnenberg, M. Hada, M. Ehara, K. Toyota, R. Fukuda, J. Hasegawa, M. Ishida, T. Nakajima, Y. Honda, O. Kitao, H. Nakai, T. Vreven, J. A. Montgomery Jr, J. E. Peralta, F. Ogliaro, M. Bearpark, J. J. Heyd, E. Brothers, K. N. Kudin, V. N. Staroverov, T. Keith, R. Kobayashi, J. Normand, K. Raghavachari, A. Rendell, J. C. Burant, S. S. Iyengar, J. Tomasi, M. Cossi, N. Rega, J. M. Millam, M. Klene, J. E. Knox, J. B. Cross, V. Bakken, C. Adamo, J. Jaramillo, R. Gomperts, R. E. Stratmann, O. Yazyev, A. J. Austin, R. Cammi, C. Pomelli, J. W. Ochterski, R. L. Martin, K. Morokuma, V. G. Zakrzewski, G. A. Voth, P. Salvador, J. J. Dannenberg, S. Dapprich, A. D. Daniels, O. Farkas, J. B. Foresman, J. V. Ortiz, J. Cioslowski, D. J. Fox, Gaussian, Inc., Wallingford CT, 2013.

[29]   A. Schaefer, H. Horn, R. Ahlrichs, *J. Chem. Phys.* **1992**, *97*, 2571–2577.

[30]   J. Tomasi, B. Mennucci, R. Cammi, *Chem. Rev.* **2005**, *105*, 2999–3009.

[31]   a) A. D. Becke, *J. Chem. Phys.* **1993**, *98*, 5648–5652; b) C. Lee, W. Yang, R. G. Parr, *Phys. Rev. B* **1988**, *37*, 785–789.

[32]   a) A. D. Becke, *Phys. Rev. A* **1988**, *38*, 3098–3100; b) J. P. Perdew, *Phys. Rev. B* **1986**, *33*, 8822–8824.

[33]   S. Grimme, *J. Comp. Chem.* **2006**, *27*, 1787–1799.

[34]   C. Adamo, V. Barone, J. Chem. Phys. **1999**, *110*, 6158–6169.

[35]   F. Neese, Orca5.0.

[36]   J. B. Gordon, J. P. McGale, J. R. Prendergast, Z. Shirani-Sarmazeh, M. A. Siegler, G. N. L. Jameson, D. P. Goldberg, *J. Am. Chem. Soc.* **2018**, *140*, 14807–14822.

Entry for the Table of Contents

Insert graphic for Table of Contents here.
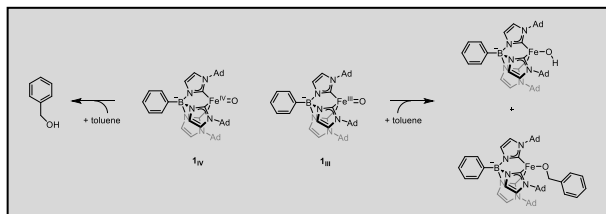
Insert text for Table of Contents here: Combined experimental and computational studies show iron(III)-oxo complexes can abstract hydrogen atoms from toluene efficiently, but thermochemically fail to do OH rebound and as such toluyl radicals are released and react separately. As a consequence iron(IV)-oxo and iron(III)-oxo generate different products in a reaction with toluene.

Institute and/or researcher Twitter usernames: The University of Manchester (@OfficialUoM); Department of Chemical Engineering and Analytical Science (@UoMSciEng); Manchester Institute of Biotechnology (@UoMMIB); Smith research group (@SmithGroupIU)